nature chemistry

Article

https://doi.org/10.1038/s41557-025-01985-8

Co-electroreduction of CO and glyoxal promotes C_3 products

Received: 19 June 2024

Accepted: 29 September 2025

Published online: 04 November 2025

Check for updates

Roham Dorakhan[1,5], Shreya Sarkar[1,5], Erfan Shirzadi[1], Hafiz Ghulam Abbas[1], Ali Shayesteh[2], Sungjin Park[1], Jianan Erick Huang[1], David Sinton[2] & Edward H. Sargent[1,3,4]

The conversion of CO_2 and CO using electricity offers a promising, sustainable approach to achieve valuable products. Although CO electroreduction to C_1 and C_2 products has seen rapid progress in efficiency and production rate, C_3 synthesis remains a major challenge. Here we show that C_3 products lie along the ethylene pathway by using a probe reactant and isotope-labelled CO. We find that glyoxal addition promotes C_3 formation while suppressing acetate/ethanol production, while itself scarcely being consumed. Spectroscopy reveals lower CO* coverage in the presence of glyoxal. Reaction-order experiments show higher coverages of CO* and of OH^- species linked to suppressing ethylene in favour of C_3. By combining both strategies to suppress ethylene formation with an abundance of OH^- and blocking acetate/ethanol formation with glyoxal, we report a high selectivity for C_3 products, including a 53% Faradaic efficiency. These insights aid the design of future catalysts for C_3 production.

The electrochemical CO reduction reaction (CORR) provides a route to upgrade CO_2 to valuable C_1 and C_2 products while avoiding carbonate/bicarbonate loss[1,2]. To date, the production of C_3 oxygenates has only achieved low selectivity and low production rates, with *n*-propanol having recently reached a Faradaic efficiency (FE) of 45% at >100 mA cm^{-2} (ref. 3). C_3 alcohols such as *n*-propanol possess a high energy density as liquid fuels, while other C_3 products, such as allyl alcohol and lactic acid, are large-scale commodity chemicals. Insights into C_3 formation pathways and key intermediates are needed to guide the rational search for catalysts and descriptors.

C_3 production involves complex reactions involving >12 electron and proton transfers. Pathways include an initial C_1–C_1 coupling step, followed by C_1–C_2 coupling; after which the ensuing C_3 intermediate undergoes proton-coupled electron transfers (PCETs) until a stable C_3 product is desorbed. The C_3 pathway(s) share intermediates with the C_2 pathway, and the resulting complex reaction landscape means that catalyst design strategies that focus on increasing C–C coupling or CO* coverage are not sufficient to provide strong selectivity to C_3 production. Indeed, one key unanswered question for the field is this: how does chain growth beyond two carbons proceed, especially along branches of the pathway that are in direct competition with C_2 products?

We focused here on identifying bifurcation points along the C_3 pathway (Fig. 1) that lead to C_2 versus C_3 production, and how tuning the reaction environment can block the competing C_2 products. Our studies were informed by previous work (Table 1) that propose intermediates for C_1–C_2 coupling. These works identify CO* as the C_1 intermediate; and they offer different C_2 intermediates, for example OCCO* (refs. 4–6) versus CH_3CO* (refs. 7,8), as the C_2 that is coupled with C_1 to form C_3. Tafel slope analysis and recent CO* coverage studies have shown the rate-determining step (RDS) for C–C coupling products to be the hydrogenation of CO* to C(H)O*, with the proton supplied from vicinal H_2O (ref. 9). Aldehydes are postulated to be intermediates in $CO_{(2)}$RR, with acetaldehyde and formaldehyde having been the object of study in recent years[8,10]. The role of acetaldehyde is less clear, with certain supporting[11] (and some suggesting a partial contribution[7])

[1]Department of Electrical and Computer Engineering, University of Toronto, Toronto, Ontario, Canada. [2]Department of Mechanical and Industrial Engineering, University of Toronto, Toronto, Ontario, Canada. [3]Department of Electrical and Computer Engineering, Northwestern University, Evanston, IL, USA. [4]Department of Chemistry, Northwestern University, Evanston, IL, USA. [5]These authors contributed equally: Roham Dorakhan, Shreya Sarkar. e-mail: ted.sargent@utoronto.ca

https://doi.org/10.1038/s41557-025-01985-8

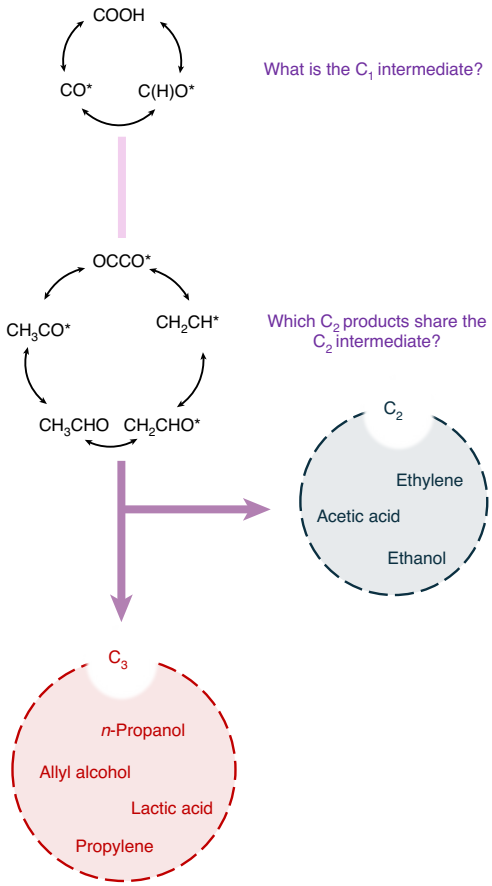

Fig. 1 | Multi-carbon $CO_{(2)}RR$ product intermediate landscape. Proposed C_1 and C_2 intermediates for C_3 production based on Table 1.

and others tending to rule out[12] its participation in C_3 formation. We set out to probe the role of CO* as the C_1 intermediate, find which C_2 and C_3 products have overlapping pathways, and generate as a result guidelines for selective increase in the production of C_3.

Results

C_3 oxygenates and ethylene lie on a shared pathway after branching from acetate and ethanol

Glyoxal, a dialdehyde, is a CORR reaction intermediate on copper, its presence supported by both DFT and experimental results[13–16], although some studies suggest it may not lie on the major ethanol-producing pathway[13,16]. To probe along the CORR mechanistic pathway on standard copper nanoparticles (Supplementary Figs. 1 and 2), we introduce [^{12}C] glyoxal in the electrolyte and simultaneously perform CORR using ^{13}CO. The isotopic labelling allows us to track carbon within the products and construct a preliminary mechanistic landscape. A gas chromatography–mass spectrometry (GC–MS) system was used to analyse the gaseous products, while liquid products were probed using NMR. A mass shift of 2 amu was observed for ethylene when labelled ^{13}CO was used in conjunction with [^{12}C]glyoxal (Supplementary Figs. 3 and 4), indicating that both carbons are labelled. Hence, both carbon atoms in ethylene stem solely from the reduction of CO and not glyoxal, and thus, glyoxal and ethylene do not lie along the same pathway.

NMR spectra (Fig. 2a–c) of liquid products from CORR using ^{13}CO or ^{12}CO and [^{12}C]glyoxal show peak splitting from ^{13}C–H interactions with a characteristic 120-Hz phase shift when using ^{13}CO. The *n*-propanol triplet at 0.7 ppm (belonging to its CH_3- protons) fully disappeared, replaced by the two double-triplet split peaks at 0.63 and 0.84 ppm, indicating that the terminal CH_3-carbon in *n*-propanol has been fully replaced with ^{13}C. The same is true for the other two carbons in *n*-propanol (double triplet at 1.38 ppm and triplet at 3.4 ppm). All three carbons in *n*-propanol hence come from CO and none come from glyoxal.

On the other hand, C_2 products (ethanol and acetate) show NMR peak splitting from ^{13}C–H, and their standard and non-split ^{12}C peaks. The carbon contribution corresponding to CH_3– of ethanol has an ~60–80% contribution from ^{13}CO, while the CH_3– carbon of acetate shows an ~50% contribution from ^{13}CO (Fig. 2d). Our findings suggest that glyoxal may share a reaction pathway with acetate and ethanol and could serve as an intermediate in their formation. While we acknowledge the possibility that the glyoxal-to-ethanol (or acetate) mechanism may differ from the conventional CORR pathway, the observed similarity in product distribution, along with previous reports identifying glyoxal as a potential $CO_{(2)}RR$ intermediate, support the assumption that its conversion to ethanol and acetate proceeds via a comparable mechanism. We therefore base our subsequent hypotheses on this mechanistic alignment.

The higher proportion of glyoxal-carbon in acetate than in ethanol may point to glyoxal being a closer intermediate to acetate; that is, glyoxal formation precedes that of acetate, and acetate precedes that of ethanol. The lack of glyoxal-carbon in C_3 products indicates that all C_3 products are along a pathway distinct from the glyoxal pathway, and thus distinct from the ethanol and acetate pathway. These results confirm the validity of glyoxal as a CORR intermediate; however, they do not translate to CO_2RR because the local HCO_3^-/CO_3^{2-} equilibrium can affect the local pH and by extension the pH-sensitive glyoxal reduction reaction (GRR). Therefore, the conclusions in this work do not confirm or refute recent studies ruling out glyoxal as a major CO_2RR intermediate along the ethanol pathway[13,16].

In sum (Fig. 2e), the pathway on which glyoxal lies leads to acetate and ethanol—and we note that it may either desorb (as does CO in CO_2RR), or, to the extent that it remains and can thus participate in further PCET steps, transform into acetate or ethanol. The early C_2 intermediate can instead take a distinct route that takes it to ethylene and C_3 oxygenates.

Effect of glyoxal addition on C_3 production and CO* coverage

We then studied how the addition of glyoxal to the electrolyte influences the partial current density and FE of C_2 and C_3 products. The electrochemical CORR performance of copper nanoparticles (Methods) in 1 M KOH solution was evaluated with (Cu–Gly) and without (copper) glyoxal addition, using a three-compartment flow electrolyser. When we analyse the electrolyte prior to application of reductive current, NMR shows no CORR products, ruling out non-electrochemical reactions as sources of the products studied in the ensuing electrochemical studies (Supplementary Fig. 5).

We first study the interconversion of species resulting from the addition of glyoxal into the electrolyte. In aqueous solutions (alkaline) and under electroreductive conditions, glyoxal may exist as a mono- or dihydrated geminal diol (or its mono- or dibasic counterpart), can undergo internal Cannizzaro disproportionation to glycolate, or may undergo external Cannizzaro disproportionation to glyoxylic acid and glycoaldehyde. Limited glycolate formation (Supplementary Fig. 6) is observed from the ^{13}C NMR study of glyoxal in solutions of varying pH (Supplementary Fig. 7). Drawing on this observation and previous literature[17–21], we constructed an interconversion map for glyoxal in our reaction medium (Supplementary Fig. 8). In this framework, glycolate, glyoxylic acid and glycoaldehyde are considered terminal products—irreversibly formed from glyoxal—while geminal diols and tetraols resulting from glyoxal hydration remain in dynamic equilibrium with the parent molecule. Consequently, mechanistic effects arising from glyoxal addition to the catholyte may involve glyoxal itself or any of its equilibrium-bound hydrated forms. This interpretation is further supported by literature reports indicating that, despite glyoxal

https://doi.org/10.1038/s41557-025-01985-8

Table 1 | List of C_3 studies with proposed intermediates, C_3 pathways and products

Study	Catalyst	$CO_{(2)}RR$ ($mA\,cm^{-2}$)	C_3 (FE, %)	Intermediates	Notes	Ref.
DFT	Cu	–	Acetone (–)	H_2CCO^*, CO^*	CCO*, HCCO* and H_3CCO^* cannot form C_3 H_2CCO^*–CO^* coupling forms C_3	37
DFT/Exp	Cu	CO_2 and CORR	Propionaldehyde, *n*-propanol	CH_2CH^*, $C(H)O^*$	CH_2CH^*-$C(H)O^*$ coupling on defects for all C_3 CH_2CHCH_2O unstable in alkaline→produces propylene CH_2CHO^* shared between C_2 and C_3	12
DFT/Exp	Cu	CO_2RR (5.5)	Propylene, *n*-propanol, allyl alcohol (<10%)	CH_2CHO^*, $COOH^*$	CH_2CHO^* coupling with $COOH^*$ to make allyl alcohol; allyl alcohol reduces to propylene	38
DFT	CuS	CO_2RR (9.9)	*n*-Propanol (15%)	$OCCO^*$, CO^*	$OCCO^*$–CO^* coupling	6
DFT	Cu	–	–	Acetaldehyde, $HCCH^*$, CO^*	Acetaldehyde–CO^* coupling forms C_3; $HCCH^*$–CO^* coupling forms C_3; more than one C_3 pathway	11
DFT	Cu	–	–	CCH^*, $CCOH^*$, CO^*	CCH^* or $CCOH^*$–CO^* coupling forms C_3	39
DFT	Cu–Ag	CORR (4.5)	*n*-Propanol (33%)	$OCCO^*$, CO^*	Screened $OCCO^*$–CO^* coupling	4,5
Exp	Cu	CORR (5)	*n*-Propanol (<10%)	Acetaldehyde, CH_3CO^*, CO^*	Acetaldehyde not on C_3 pathway; high CO^* coverage lowers C_3	8
Exp	Cu	CORR (9)	*n*-Propanol (<10%)	Acetaldehyde, CH_3CO^*, CO^*	Acetaldehyde in one-third of produced C_3; CH_3CO^*–CO^* coupling forms C_3	7

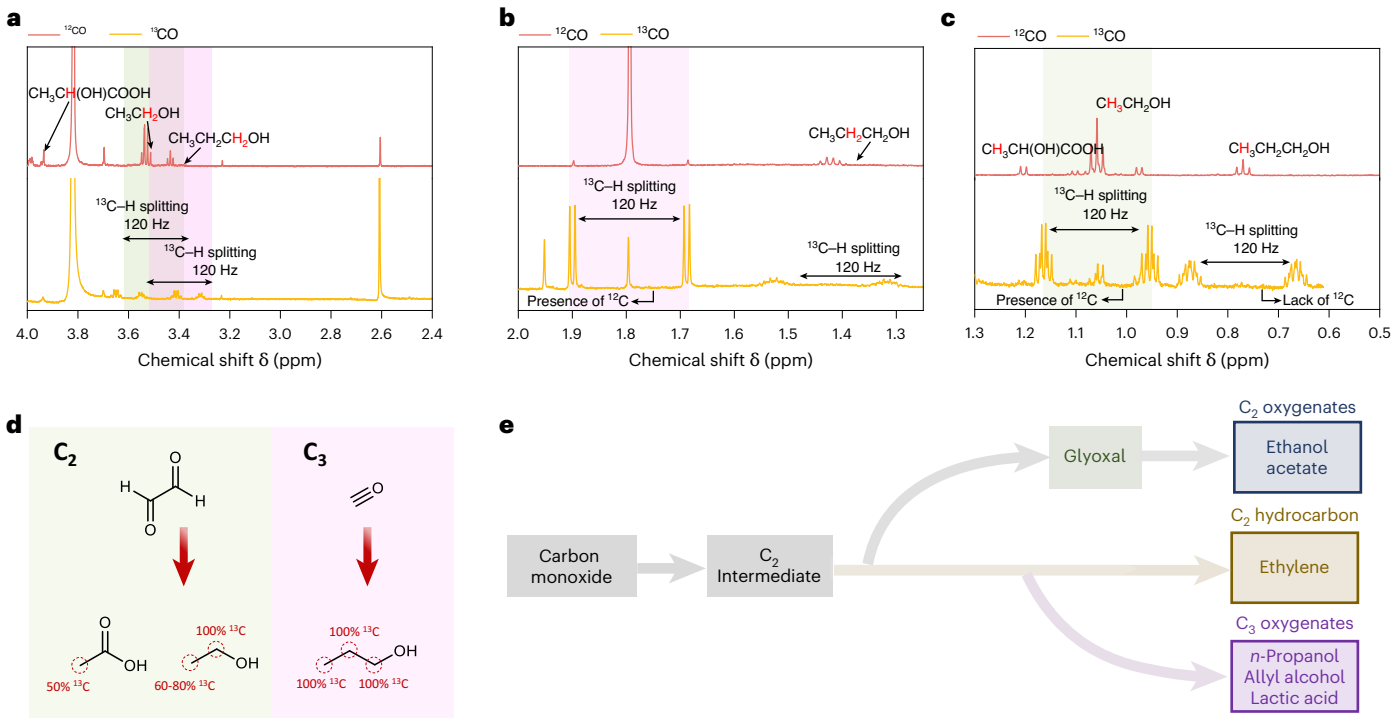

Fig. 2 | Carbon tracing in ethanol, acetate and *n*-propanol using NMR analysis of ^{13}CO, ^{12}CO and [^{12}C]glyoxal. a–**c**, NMR spectrum of liquid products produced by ^{13}CO reduction in 1 M KOH and 50 mM glyoxal where each panel shows a different chemical shift range: 2.4–4.0 ppm (**a**), 1.25–2.0 ppm (**b**) and 0.5–1.3 ppm (**c**). NMR peak splitting showing the presence of both ^{12}C and ^{13}C atoms in ethanol while showing the presence of only ^{13}C in propanol (**a**,**c**); NMR peak splitting showing the presence of both ^{12}C and ^{13}C atoms in acetate (**b**). **d**, Schematic showing the product distribution from CO and glyoxal as determined from isotope-labelling experiments. **e**, Preliminary mechanistic pathways based on an isotope-labelling study using glyoxal and ^{13}CO.

predominantly existing in its hydrated state in aqueous media, its aldehyde form remains chemically accessible and reactive[21].

The pH under which the GRR was examined (1 M KOH) is much higher than that used in other reports[22,23], in which no GRR products were observed and the reactions were fully dominated by the hydrogen evolution reaction (HER). It is possible that this difference in pH is key in not allowing GRR to proceed, especially since the interconversions of glyoxal-derived species are very pH sensitive.

We studied the effect of glycolate (the most abundant form of glyoxal side product, and one found in our studies) and its coverage on the reaction pathways of common products (ethylene and ethanol) using density functional theory (DFT) (Supplementary Note 1 and

https://doi.org/10.1038/s41557-025-01985-8

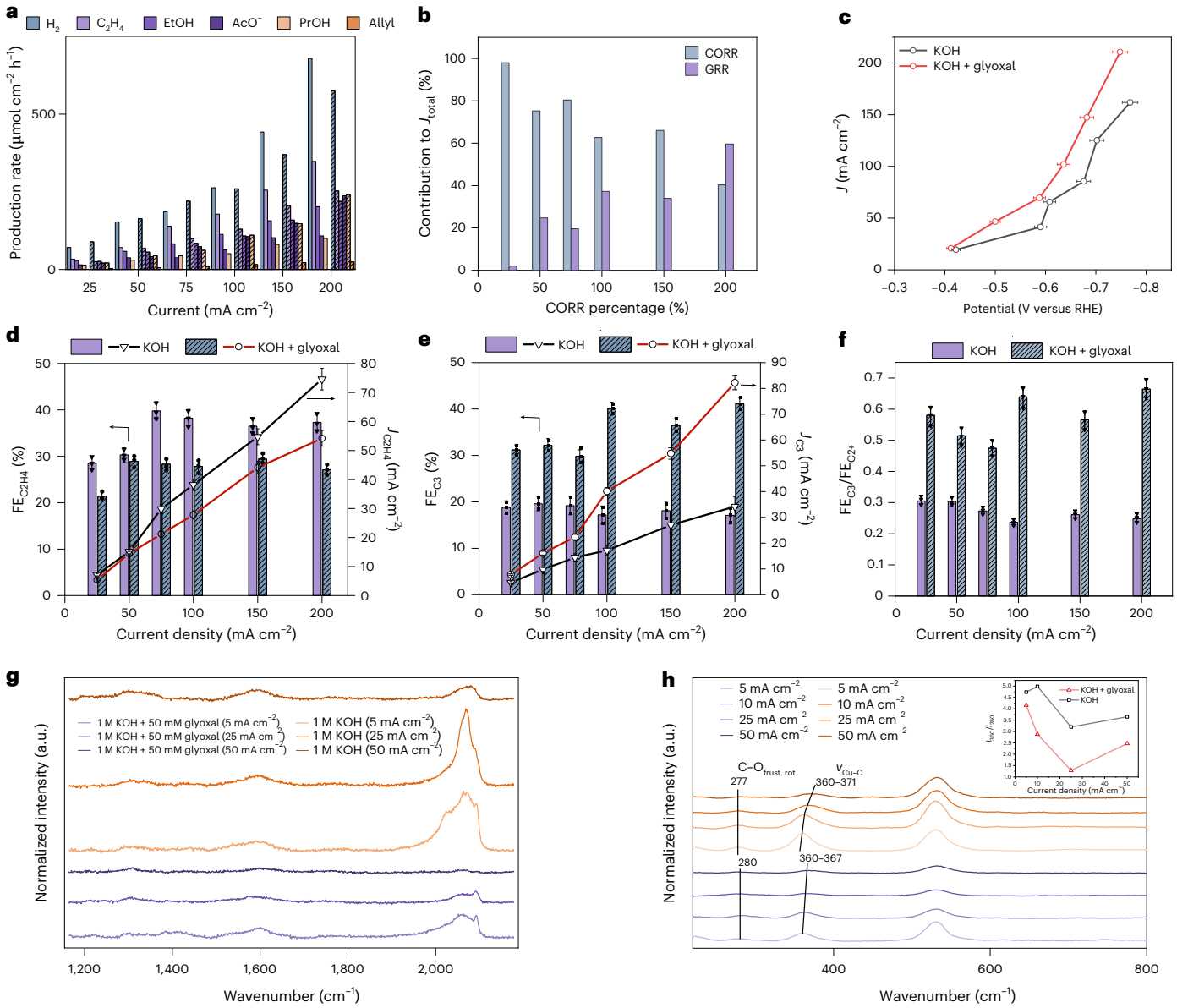

Fig. 3 | Effect of glyoxal addition on C_2 and C_3 product formation and operando Raman spectra. a, Production rate of CORR products with (hashed columns) and without (solid columns) glyoxal addition to the electrolyte (50 mM). **b**, Calculation of total FE considering various percentages of CO and glyoxal reduction. **c**, Partial current densities of products for Cu–Gly and copper samples under different potentials. Error bars represent the s.d. of potentials (>60 data points collected in one experiment) during the constant-current electrolysis. **d**, Ethylene FEs and partial current densities on different electrodes at various current densities. Error bars represent the s.d. of three independent samples. **e**, C_3 FEs and partial current densities on different electrodes at various current densities. Error bars represent the s.d. of three independent samples. **f**, Comparison of FE_{C3}/ FE_{C2} ratios on different electrodes at various current densities. **g**,**h**, Raman spectra of copper nanoparticles in 1 M KOH with (**g**) and without (**h**) 50 mM glyoxal addition in the electrolyte. Inset: peak intensity ratio of the peaks centred at 280 cm^{-1} and 360 cm^{-1} across all current densities.

Supplementary Figs. 9–15) and found adsorbed glycolate to have little effect on the energetic pathways of ethylene and ethanol formation, even under higher coverages. Experimentally, the addition of glycolate (and other potential candidate compounds) did not result in any CORR-product formation enhancement and only contributed to the increase in the HER (Supplementary Fig. 16).

Cu–Gly showed an increase in total FE (the FE calculated on the premise of the eight-electron reaction from CO to ethanol) compared with copper, in some cases above 100%, and hence, the production rate of each component is compared instead (Fig. 3a–f and Supplementary Fig. 17). Contributions from both the CORR and the GRR can transform glyoxal to ethanol and acetate as indicated by isotope labelling (Fig. 2e), and a concomitant effect on ethylene production and its suppression (Fig. 3a). Because glyoxal has a lower oxidation state than CO, fewer electrons are required for its conversion than CO. The GRR-to-CORR ratio is estimated as the ratio resulting in $J_{GRR} + J_{CORR}$ equalling the current density, and the results show that the GRR is more dominant at higher currents (Fig. 3b). We account for this by noting the CO shortage at large current densities (50–200 mA cm^{-2}), enabling GRR to take over. The overall current density increases (Fig. 3c) with the addition of glyoxal, with additional C_3 products such as allyl alcohol and lactic acid emerging (Fig. 2a (allyl alcohol and lactic acid are grouped under 'Allyl') and Supplementary Fig. 18). It is notable that no direct glyoxal reduction is observed when the CO is replaced with inert N_2 (Supplementary Figs. 19 and 20): CO is thus a co-reactant—one that suppresses the HER and allows glyoxal to participate in the reduction

reaction. It is notable that the consumption of glyoxal through the GRR poses an important economic challenge.

Addition of glyoxal resulted in a decrease in the ethylene FE across all current densities, accompanied by an increase in C_3 FE (Fig. 3d,e). The ratio of C_3 FE to total C_{2+} FE ($FE_{C3/C2+}$) increased by a factor of ~2× (Fig. 3f); that is, C_3 product formation is promoted by the addition of glyoxal. This agrees with the picture of Fig. 3e in which ethylene and C_3 oxygenate share a common pathway.

To investigate further the role of glyoxal, we performed operando surface-enhanced Raman spectroscopy on copper nanoparticles with 1 M KOH electrolytes with and without glyoxal addition (Fig. 3g,h). Spectra obtained at lower current densities show higher peak intensities throughout; at higher current densities, CO* and surface species are consumed, lowering their prominence in the spectra. The CO* vibrational frequencies in the 2,000- to 2,100-cm^{-1} range correspond to C≡O stretching, the features in the 275- to 280-cm^{-1} range are due to the frustrated rotation of the C–O bond in CO*, and the 360-cm^{-1} peak is attributed to the stretching vibrational frequency of Cu–C (Fig. 3h)[24–26]. The CO* surface coverage (θ_{CO*}) and the intensity ratios of the 360- and 280-nm peaks have been shown to be correlated[27] (Fig. 3h). The intensity ratios of the 360- to 280-cm^{-1} peaks (I_{360}/I_{280}) decrease with increasing current densities (Fig. 3h, inset), a result of CO depletion at those higher rates. Addition of glyoxal to the electrolyte lowers the intensity ratio across all current densities, indicating lower CO* coverage. Hence, glyoxal can adsorb on the surface and compete with CO* for adsorption sites.

C_3 production dependence on metal cations, CO coverage and glyoxal concentration

Glyoxal has exhibited two effects on the CORR mechanism: (1) an increase in C_3 FE, and (2) a decrease in CO* coverage. We now delve into understanding the dependency of C_3 formation rate on reaction conditions including metal cations, CO* coverage and glyoxal concentration. Metal cation identity substantially influenced both the HER and the C_3/C_2 ratio (Supplementary Figs. 21 and 22) with K^+ exhibiting the lowest HER and the highest C_3 FE. Concentration-dependence experiments with K^+ showed that higher concentrations in the outer Helmholtz plane resulted in C_2H_4 suppression (Supplementary Fig. 23). Anion identity also played a crucial role, with OH^- enhancing the CORR and liquid oxygenate production (Supplementary Fig. 24)[9,28,29]. Hence, higher concentrations of K^+ suppress C_2H_4 formation, and when paired with OH^- as the anion, maximize the CORR and liquid oxygenate formation rates.

To elucidate how CO* influences C_2 and C_3 pathways, we conducted reaction-order experiments, varying the CO partial pressure in the presence of glyoxal (Fig. 4a–c). The total current density is dominated by the sum of HER and C_{2+} production (C_1 FE < 1%), resulting in the HER and C_{2+} reaction orders following opposite trends. C_{2+} production increases as the CO pressure is lowered from 1 bar, passing through a CO poison region. Even lower pressures (P_{CO} < 0.4 bar in 1 M KOH and P_{CO} < 0.2 bar in 3 M KCl) cause C_{2+} production to cease abruptly. The RDS of C–C coupled products involves hydrogenation of CO* via a physiosorbed H_2O molecule (H_2O*), with each CO* displacing n adjacent water molecules such that $n\theta_{CO*} + \theta_{H2O*} = 1$, resulting in maximum rates being achieved when the two terms are equal ($r_{max} = kn\theta_{CO*}\theta_{H2O*}$, where $n\theta_{CO*} = \theta_{H2O*}$)[9,27,30]. Under 1 bar, $n\theta_{CO*} > \theta_{H2O*}$, and lowering θ_{CO*} (by lowering the pressure) causes an increase in $kn\theta_{CO*}\theta_{H2O*}$ and the CORR rate. Below a certain pressure, CO* coverage is lowered drastically, stopping the CORR and causing a sharp increase in the HER.

Production of ethylene follows a different reaction order depending on the electrolyte used, with KCl causing a rise in overall ethylene production compared with KOH (Fig. 4b). Ethylene production increases with decreasing pressure in KCl electrolyte, while in KOH, it initially decreases before increasing simultaneously with HER. The selectivity-determining step (SDS) for ethylene has been suggested to involve a 3-copper (copper) anchored intermediate, where at lower CO pressures competition for active sites with CO* is reduced resulting in a negative order relation, while in the presence of OH^-, this competition is dampened and a positive reaction order is observed (<0.4 bar, Fig. 4b)[31].

The liquid oxygenate (and C_3) production is maximized in the ethylene-suppressing KOH electrolyte, with a positive-order dependence of C_3 oxygenates on CO pressure (Fig. 4c). Whereas glyoxal can act on the acetate/ethanol pathway, partially blocking it and directing the reaction towards the ethylene/C_3 path, KOH can act directly on the ethylene/C_3 pathway, preferentially switching selectivity away from ethylene, while C_3 products that lie along the ethylene path are not suppressed. The positive order dependence of C_3 products on CO pressure also suggests that high coverages of CO* are needed for C_3 production, suggesting CO* is the critical C_1 intermediate in the C_1–C_2 coupling reaction.

We move to KOH electrolytes to suppress ethylene and study the effect of glyoxal concentration (Fig. 4d–f). A zero-order dependence on C_{2+} products is observed in 6 M KOH, whereas a negative-order dependence (positive with respect to HER) in 1 M KOH is linked to the increased alkalinity influencing the glyoxal-to-glycolate transformation and lowering glyoxal concentration in the 6 M case (Fig. 4d). Higher KOH concentrations suppress ethylene more as the reaction pathways of both ethylene and C_3 become glyoxal independent (zero-order dependence) (Fig. 4e). The influence of glyoxal influence on blocking the acetate/ethanol pathway requires a small amount of glyoxal and higher concentrations are redundant. The dependence of C_3 and C_2 product formation on water concentration is summarized in Supplementary Figs. 25 and 26. Water concentration is modulated using dimethylsulfoxide (DMSO) and a positive dependence for C_{2+} and C_3 production is observed, consistent with the H_2O being involved in the RDS of the C_{2+} pathway, but not affecting selectivity beyond the RDS[9].

The distinct [KOH]–P_{CO} regimes (Fig. 4g–i) and current density–[KOH] regimes (Supplementary Fig. 27) for the HER, ethylene and C_3 oxygenate can be visualized on a contour plot. These plots offer visual guidance on which operating conditions to pursue depending on the product of choice.

Maximizing C_3 oxygenate production

Having established that: (1) glyoxal suppresses the acetate/ethanol pathway and enhances the ethylene/C_3 path, (2) KOH suppresses ethylene formation while not affecting C_3 production, (3) high CO pressures are required to increase C_3 production and (4) a minimum of 100 mM glyoxal is needed to enhance C_3 FE under high KOH concentration, we move to optimize C_3 FE. We increase the KOH concentration from 1 M to 10 M, while maintaining a glyoxal concentration of 150 mM and a CO partial pressure of 1 bar (Fig. 5a and Supplementary Fig. 28). An increase in C_3 FE is observed with *n*-propanol, allyl alcohol and lactic acid as the dominant C_3 oxygenate products (Fig. 5a,b), at all current densities (75–200 mA cm^{-2}). Lower currents (75 mA cm^{-2}) show a near first-order increase in C_3 from 1 M to 6 M KOH, and a close to zero-order increase above 6 M KOH. The near first-order reaction dependence on KOH is maintained at 100 and 150 mA cm^{-2}, whereas higher currents of 200 mA cm^{-2} cause an initial decrease in C_3 formation rates, until a first-order dependence is once again observed at >3 M KOH. Locally, more OH^- species are produced at higher current densities, causing a more immediate ethylene suppression effect noticeable at lower KOH concentrations, while at 200 mA cm^{-2}, CO transport limitation starts to decrease CO* coverage. Using this approach, C_3 oxygenate FEs of 63% at 75 mA cm^{-2} and 58% at 100 mA cm^{-2} are obtained. These correspond to ~53% and ~50% *n*-propanol FE at the respective current densities.

Building upon previous observations, we move to construct a C_3 formation mechanism (Fig. 5c). The RDS for C–C coupling products starts from the hydrogenation of CO*, forming the C_1 intermediate CHO* (ref. 9). The cross-coupling of CO* and CHO* produces the OCCHO* intermediate. This intermediate is associated with C_2 products on copper, and from theory is a stable C_2 intermediate[32–36].

https://doi.org/10.1038/s41557-025-01985-8

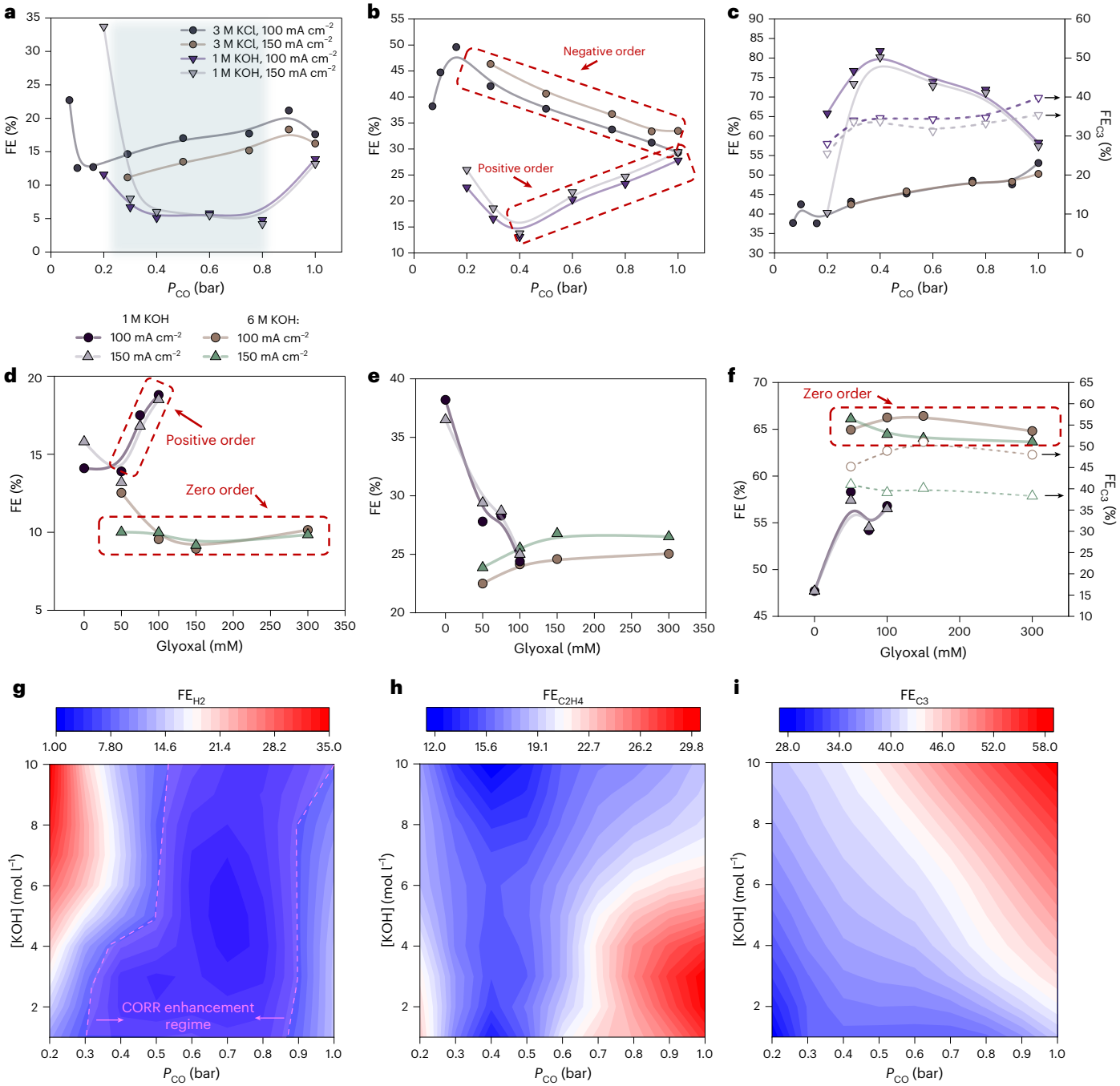

Fig. 4 | Dependence of C_3 production on CO and glyoxal concentration. a–c, Hydrogen (**a**), ethylene (**b**) and liquid oxygenate and C_3 oxygenate FEs (**c**) at varying CO partial pressures in electrolytes containing 50 mM glyoxal. The legend in **a** corresponds to data from **a**–**c**. **d**–**f**, Hydrogen (**d**), ethylene (**e**) and liquid oxygenate and C_3 oxygenate FEs (**f**) at varying glyoxal concentrations in 1 M and 6 M KOH electrolytes. The legend in **d** corresponds to data from **d**–**f**. **g**–**i**, Hydrogen (**g**), ethylene (**h**) and C_3 oxygenate FEs (**i**) at varying CO partial pressures and KOH concentrations at 100 mA cm^{-2} in electrolytes containing 50 mM glyoxal.

Glyoxal is a desorbing intermediate along the ethanol and acetate pathway. Isotope-labelling experiments show that the ethylene pathway bifurcates from that of ethanol and acetate prior to the formation of glyoxal. This presents the first bifurcation point along the C_2 product pathways. OCCHO* undergoes one or multiple PCET steps to produce the selectivity-determining intermediate I*. The ethylene and acetate/ethanol pathways can be accessed via two distinct intermediates (Y* and X*, respectively) originating from I*, making this the SDS in C_2 products. The equilibrated adsorption of glyoxal is present along the acetate/ethanol pathway, while the ethylene-specific intermediate performs further cross-coupling with a C_1 intermediate to produce C_3. Reaction-order experiments show a positive order relation between CO* coverage and C_3 production, where a sufficiently high θ_{CO^*} maximized C_3 production. We identify CO* to be the C_1 intermediate required for C_1–C_2 coupling. Glyoxal can change the reaction pathway towards more C_3 products by shifting the quasi-equilibrated Y* → glyoxal* equilibrium towards Y* per the Le Chatelier's principle, causing the quasi-equilibrated I* → Y* step to also be pushed backwards and lower Y* coverage. The C_2 SDS is essentially shifted away from the acetate/ethanol path (Y*) back into the ethylene/C_3 pathway (X*). Carrying

https://doi.org/10.1038/s41557-025-01985-8

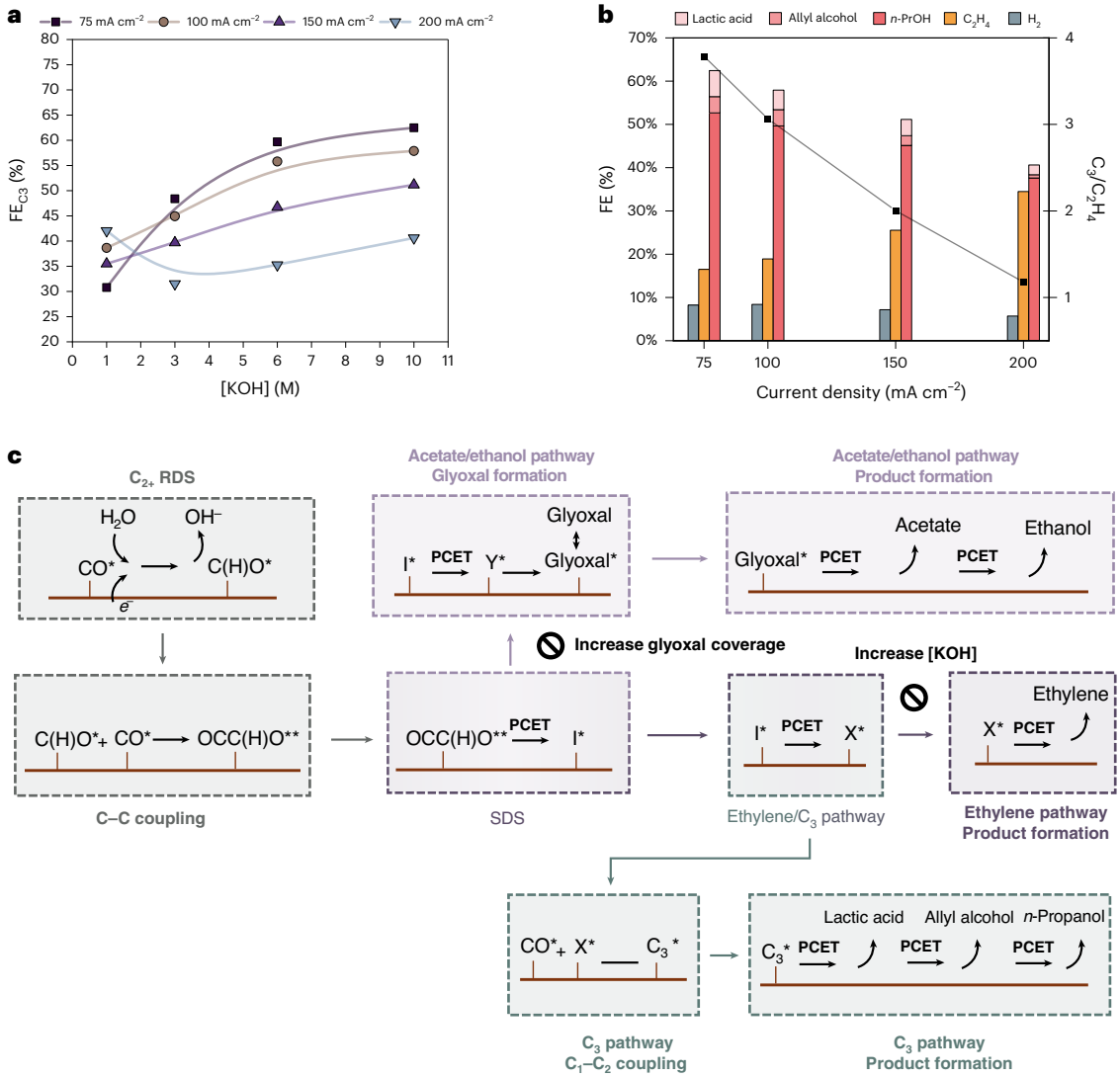

Fig. 5 | C$_3$ product maximization and C$_3$ production mechanism. a, C$_3$ FE (*n*-propanol, allyl alcohol and lactic acid) on copper nanoparticles and 150 mM glyoxal (except 1 M KOH where 50 mM glyoxal was used). **b**, FE of C$_3$ (*n*-propanol, allyl alcohol and lactic acid), hydrogen and ethylene in 10 M KOH and 150 mM glyoxal. **c**, Proposed reaction mechanism for C$_3$ oxygenate formation on copper nanoparticles.

out the reaction under conditions that suppress ethylene formation, for example, high KOH concentrations, when glyoxal is used to suppress the acetate/ethanol path, substantially enhances C$_3$ production (Fig. 5b,c).

Leveraging the Le Chatelier's principle to steer selectivity relies on the ability of an added species to perturb elementary-step equilibria that influence upstream branching points in the reaction network. Glyoxal occupies a mechanistically central position—intermediate between early C–C coupling steps and the formation of more reduced products—and remains in dynamic equilibrium with several surface-accessible intermediates. As such, changes in its concentration can shift upstream equilibria and alter the distribution of surface-bound species in a way that blocks ethanol and acetate formation and favours pathways leading to C$_3$ products.

In contrast, acetaldehyde—another proposed intermediate in the CO$_{(2)}$RR—is more hydrogenated and lies further downstream in the reduction sequence. It is not known to appreciably readsorb or participate in reversible surface equilibria on copper, and instead behaves more like a terminal product. As a result, perturbing its concentration has limited feedback on upstream steps and minimal influence on product selectivity. This is consistent with our experimental findings, which show that the addition of acetaldehyde does not enhance C$_3$ product formation (Supplementary Fig. 16). Thus, while the conceptual framework we propose—modulating intermediate concentrations to influence selectivity—is general, its applicability depends on the mechanistic position and the surface accessibility of the species in question. Glyoxal is effective in this regard because it is sufficiently upstream and equilibrated to shift the reaction landscape, whereas acetaldehyde is not.

Discussions

This study investigates C$_3$ formation in CORR on copper nanoparticles using probe reactants, isotopic labelling, reaction-order experiments and operando Raman spectroscopy. Isotope labelling reveals glyoxal to be a desorbing intermediate strictly on the ethanol/acetate pathway, indicating a pathway separation from ethylene. Glyoxal addition blocks the acetate/ethanol pathway, enhances selectivity for *n*-propanol and generates new C$_3$ products such as allyl alcohol and lactic acid. Surface-enhanced Raman spectroscopy shows glyoxal reducing CO* coverage, competing with CO* for adsorption, while OH$^-$ anions suppress ethylene formation. Reaction-order analysis on CO exhibits a positive dependence in KOH electrolytes but a negative dependence

in KCl. The coadsorption effect of glyoxal enhances C_3 production moderately, with a negative order dependence at higher concentrations. Screening various KOH concentrations identifies kinetic regimes favouring C_3 FE (~65%). The mechanistic landscape reveals CO* to be the critical C_1 intermediate for C_1–C_2 coupling, with the C_2 intermediate being found exclusively along the ethylene pathway. These insights aid in designing catalysts favouring C_3 production, with potential applications in other CORR products and mechanistic pathway investigations.

Online content

Any methods, additional references, Nature Portfolio reporting summaries, source data, extended data, supplementary information, acknowledgements, peer review information; details of author contributions and competing interests; and statements of data and code availability are available at https://doi.org/10.1038/s41557-025-01985-8.

References

1. Jouny, M., Hutchings, G. S. & Jiao, F. Carbon monoxide electroreduction as an emerging platform for carbon utilization. *Nat. Catal.* **2**, 1062–1070 (2019).
2. Service, R. F. Hunt for renewable plastics clears a hurdle. *Science* https://doi.org/10.1126/science.371.6532.873 (2021).
3. Phong Duong, H. et al. Silver and copper nitride cooperate for CO electroreduction to propanol. *Angew. Chem. Int. Ed.* https://doi.org/10.1002/anie.202310788 (2023).
4. Wang, X. et al. Efficient electrosynthesis of n-propanol from carbon monoxide using a Ag–Ru–Cu catalyst. *Nat. Energy* https://doi.org/10.1038/s41560-021-00967-7 (2022).
5. Pang, Y. et al. Efficient electrocatalytic conversion of carbon monoxide to propanol using fragmented copper. *Nat. Catal.* **2**, 251–258 (2019).
6. Peng, C. et al. Double sulfur vacancies by lithium tuning enhance CO_2 electroreduction to *n*-propanol. *Nat. Commun.* **12**, 1–8 (2021).
7. Chang, X., Malkani, A., Yang, X. & Xu, B. Mechanistic Insights into electroreductive C–C coupling between CO and acetaldehyde into multicarbon products. *J. Am. Chem. Soc.* **142**, 2975–2983 (2020).
8. da Silva, A. H. M., Lenne, Q., Vos, R. E. & Koper, M. T. M. Competition of CO and acetaldehyde adsorption and reduction on copper electrodes and its impact on *n*-propanol formation. *ACS Catal.* **13**, 4339–4347 (2023).
9. Chang, X. et al. C–C coupling is unlikely to be the rate-determining step in the formation of C_{2+} products in the copper-catalyzed electrochemical reduction of CO. *Angew. Chem. Int. Ed.* **61**, e202111167 (2022).
10. Bertheussen, E. et al. Acetaldehyde as an intermediate in the electroreduction of carbon monoxide to ethanol on oxide-derived copper. *Angew. Chem. Int. Ed.* **55**, 1450–1454 (2016).
11. Tang, M. T., Peng, H. J., Stenlid, J. H. & Abild-Pedersen, F. Exploring trends on coupling mechanisms toward C_3 product rormation in $CO_{(2)}R$. *J. Phys. Chem. C* **125**, 26437–26447 (2021).
12. Pablo-García, S. et al. Mechanistic routes toward C_3 products in copper-catalysed CO_2 electroreduction. *Catal. Sci. Technol.* **12**, 409–417 (2022).
13. Delmo, E. P. et al. The role of glyoxal as an intermediate in the electrochemical CO_2 reduction reaction on copper. *J. Phys. Chem. C* https://doi.org/10.1021/acs.jpcc.3c00589 (2023).
14. Calvinho, K. U. D. et al. Surface hydrides on Fe_2P electrocatalyst reduce CO_2 at low overpotential: steering selectivity to ethylene glycol. *J. Am. Chem. Soc.* **143**, 21275–21285 (2021).
15. Tamura, J. et al. Electrochemical reduction of CO_2 to ethylene glycol on imidazolium ion-terminated self-assembly monolayer-modified Au electrodes in an aqueous solution. *Phys. Chem. Chem. Phys.* **17**, 26072–26078 (2015).
16. Reichert, A. M., Piqú, O., Parada, W. A., Katsounaros, I. & Calle-Vallejo, F. Mechanistic insight into electrocatalytic glyoxal reduction on copper and its relation to CO_2 reduction. *Chem. Sci.* https://doi.org/10.1039/d2sc03527h (2022).
17. Hazra, M. K., Francisco, J. S. & Sinha, A. Hydrolysis of glyoxal in water-restricted environments: formation of organic aerosol precursors through formic acid catalysis. *J. Phys. Chem. A* **118**, 4095–4105 (2014).
18. Wu, Z. et al. Study on the soy protein-based adhesive cross-linked by glyoxal. *J Renew Mater* **9**, 205–218 (2020).
19. Bedford, C. T., Fallah, A., Mentzer, E. & Williamson, F. A. The first characterisation of a glyoxal–hydrogen sulfide adduct. *Chem. Commun.* https://doi.org/10.1039/C39920001035 (1992).
20. Michailoudi, G. et al. Aqueous-phase behavior of glyoxal and methylglyoxal observed with carbon and oxygen K-edge X-ray absorption spectroscopy. *Atmos. Chem. Phys.* **21**, 2881–2894 (2021).
21. Kliegman, J. M., Whipple, E. B., Ruta, M. & Barnes, R. K. Glyoxal derivatives. IV. 2-Dimethoxymethyl-4,5-dimethoxy-1,3-dioxolane and 2,2′-bis(4,5-dimethoxy-1,3-dioxolane). *J. Org. Chem.* **37**, 1276–1279 (1972).
22. Schouten, K. J. P., Kwon, Y., Van Der Ham, C. J. M., Qin, Z. & Koper, M. T. M. A new mechanism for the selectivity to C_1 and C_2 species in the electrochemical reduction of carbon dioxide on copper electrodes. *Chem. Sci.* **2**, 1902–1909 (2011).
23. Reichert, A. M., Piqué, O., Parada, W. A., Katsounaros, I. & Calle-Vallejo, F. Mechanistic insight into electrocatalytic glyoxal reduction on copper and its relation to CO_2 reduction. *Chem. Sci.* **13**, 11205–11214 (2022).
24. Zhao, Y. et al. Speciation of Cu surfaces during the electrochemical CO reduction reaction. *J. Am. Chem. Soc.* **142**, 9735–9743 (2020).
25. De Ruiter, J. et al. Probing the dynamics of low-overpotential CO_2-to-CO activation on copper electrodes with time-resolved Raman spectroscopy. *J. Am. Chem. Soc.* **144**, 15047–15058 (2022).
26. Wu, Z. Z. et al. Identification of Cu(100)/Cu(111) interfaces as superior active sites for CO dimerization during CO_2 electroreduction. *J. Am. Chem. Soc.* **144**, 259–269 (2022).
27. Zhan, C. et al. Revealing the CO coverage-driven C–C coupling mechanism for electrochemical CO_2 reduction on Cu_2O nanocubes via operando Raman spectroscopy. *ACS Catal.* **11**, 7694–7701 (2021).
28. Chang, X., Zhao, Y. & Xu, B. P. H. Dependence of Cu surface speciation in the electrochemical CO reduction reaction. *ACS Catal.* **10**, 13737–13747 (2020).
29. Li, J. et al. Electrokinetic and in situ spectroscopic investigations of CO electrochemical reduction on copper. *Nat. Commun.* **12**, 1–11 (2021).
30. Kong, X. et al. Understanding the effect of *CO coverage on C–C coupling toward CO_2 electroreduction. *Nano Lett.* https://doi.org/10.1021/acs.nanolett.2c00945 (2022).
31. Li, J. et al. Constraining CO coverage on copper promotes high-efficiency ethylene electroproduction. *Nat. Catal.* **2**, 1124–1131 (2019).
32. Gauthier, J. A., Lin, Z., Head-Gordon, M. & Bell, A. T. Pathways for the formation of C_{2+} products under alkaline conditions during the electrochemical reduction of CO_2. *ACS Energy Lett.* **19**, 1679–1686 (2022).
33. Shah, A. H. et al. The role of alkali metal cations and platinum-surface hydroxyl in the alkaline hydrogen evolution reaction. *Nat. Catal.* **5**, 923–933 (2022).

34. Todorova, T. K., Schreiber, M. W. & Fontecave, M. Mechanistic understanding of CO_2 reduction reaction (CO_2RR) toward multicarbon products by heterogeneous copper-based catalysts. *ACS Catal.* **10**, 1754–1768 (2020).
35. Ma, M. et al. Local reaction environment for selective electroreduction of carbon monoxide. *Energy Environ. Sci.* https://doi.org/10.1039/D1EE03838A (2022).
36. Santatiwongchai, J., Faungnawakij, K. & Hirunsit, P. Comprehensive mechanism of CO_2 electroreduction toward ethylene and ethanol: the solvent effect from explicit water–Cu(100) interface models. *ACS Catal.* **11**, 9688–9701 (2021).
37. Chang, C. C., Ku, M. S., Lien, W. H. & Hung, S. F. Unveiling the bonding nature of C_3 intermediates in the CO_2 reduction reaction through the oxygen-deficient Cu_2O(110) surface—a DFT study. *J. Phys. Chem. C* **126**, 5502–5512 (2022).
38. Gao, J. et al. Electrochemical synthesis of propylene from carbon dioxide on copper nanocrystals. *Nat. Chem.* https://doi.org/10.1038/s41557-023-01163-8 (2023).
39. Chan, Y., Te, Huang, I. S. & Tsai, M. K. Enhancing C–C bond formation by surface strain: a computational investigation for C_2 and C_3 intermediate formation on strained Cu surfaces. *Phys. Chem. Chem. Phys.* **21**, 22704–22710 (2019).

Methods

Chemicals

Glyoxal (40 wt% in H_2O), methanol (ACS reagent grade, >99.8%), DMSO (ACS reagent grade >99.9%), lithium hydroxide (ACS reagent grade 98%), sodium hydroxide (ACS reagent grade 98%) and potassium hydroxide (semiconductor grade 99.99%) were purchased from Sigma Aldrich. Copper nanoparticles (99.8%, 25 nm) were purchased from US Research Nanomaterials. Nafion solution (D520, 5 wt%), carbon paper (Freudenberg H23C8), nickel foam and bipolar membrane (Fumasep FBM) were purchased from Fuel Cell Store. All chemicals were used as received. The aqueous solutions were prepared using deionized water with a resistivity of 18.2 MΩ·cm.

Preparation of gas diffusion electrodes

Copper nanoparticles were dispersed in a mixture of methanol and Nafion solution and left under ultrasonication for at least 30 min. The catalyst ink composition was 3.6 mg_{Cu} ml_{ink}^{-1} and 5 μl_{Nafion} 5 wt% mg_{Cu}^{-1}. The ink was spray coated on a carbon paper gas diffusion layer (Freudenberg H2C38) with a copper nanoparticle loading of 2 mg cm^{-2} to prepare the copper electrode. The electrodes were left under room conditions overnight before the electrochemical measurements were conducted.

Flow-cell assembly

The flow-cell set-up consists of three compartments: the anolyte, catholyte and gas-flow chambers. The geometric area of the electrode window was 1 × 1 cm^2. The cathode was clamped between the catholyte and gas-flow chambers, with the catalyst side facing the catholyte. A nickel foam was used as the anode, and an Ag/AgCl electrode (3 M KCl, CHI Instruments) was used as the reference electrode in the catholyte chamber. The catholyte and anolyte chambers were separated by a Fumasep bipolar membrane. The catholyte and anolyte were circulated by peristaltic pumps at a constant rate of ~20 ml min^{-1}.

Electrochemical CO reduction measurement

The electrochemical CORR was performed in a flow cell. Carbon monoxide (Linde, 99.95%) was purged in the flow cell gas chamber using a mass flow controller (Sierra SmartTrack100). The CO flow rate was set to 25–40 standard cubic centimetre per minute (sccm). Electrochemical reactions were performed using an electrochemical workstation (Autolab PGSTAT302N) connected to a current booster (Metrohm Autolab, 10 A). Electrode potentials were rescaled to the reversible hydrogen electrode (RHE) reference by:

$$E_{\text{vs RHE}} = E_{\text{Ag/AgCl}} + 0.220\,\text{V} + 0.059 \times \text{pH}$$

Electrochemical impedance spectroscopy measurements using an Autolab PGSTAT302N electrochemical workstation measured the cell resistance to be 4.08 Ω. *iR* corrections to the potential were then performed using the equation:

$$E_{iR\,\text{free}} = E_{Ag/AgCl} - 0.85R_{cell}i_{\text{cell}}$$

where $E_{iR\,\text{free}}$ is the corrected potential at the cathode, $E_{\text{Ag/AgCl}}$ is the applied potential and i_{cell} is the total current (a negative value at the cathode). A correction factor of 0.85 was used due to the 1 M KOH electrolyte's high conductance and low voltage drop across the electrolyte.

The copper nanoparticle-modified carbon-based gas diffusion layer was used as the cathode. Glyoxal (50 mM) was added to the catholyte for the CORR on Cu–Gly. The volumes of catholyte and anolyte used for circulation were 25 ml. The current densities reported are based on geometric surface area.

Electrochemical reduction product measurement

The gas products were collected from the gas outlet of the flow cell and injected into a gas chromatograph (Shimadzu GC-2014) for gas quantification. The gas chromatograph was equipped with a thermal conductivity detector (TCD) for the detection of H_2 and CO signals, and a flame ionization detector (FID) for the detection of CH_4 and C_2H_4 signals. The gas chromatograph was equipped with a molecular sieve (5 Å) and Carboxen-1000 column upstream from the TCD and FID, respectively. Argon (Linde, 99.999%) was used as the carrier gas. The FE of the gas products was calculated using the following equation:

$$\text{FE}_i = y_i V z_i F \frac{P_0}{RT} j_{\text{total}}$$

where FE_i is the Faradaic efficiency of product i, y_i is the volumetric fraction of the gas product, V is the outlet gas flow rate in sccm, z_i is the number of electrons associated with producing one molecule of product from CO, F is the Faraday constant, P_0 is the atmospheric pressure, R is the ideal gas constant, T is the temperature and j_{total} is the total current density.

The liquid products were analysed using ^{1}H NMR spectroscopy (600 MHz Agilent DD2 NMR spectrometer) with water suppression. DMSO was used as the reference standard and deuterium oxide as the lock solvent. The FE of liquid products were calculated using the equation:

$$\text{FE}_i = n_i z_i F \frac{1}{Q_{\text{total}}}$$

where n_i is the number of moles of liquid product i and Q_{total} is the total charge passed through the cell prior to liquid sampling.

Electrochemical ^{13}CO isotope-labelling experiment

The isotope-labelling experiments were conducting using ^{13}CO (>99 at.% ^{13}C, Sigma Aldrich) and [^{12}C]glyoxal. Carbon monoxide was introduced to the gas chamber of the flow cell. Glyoxal was added to the electrolyte solution to reach a concentration of 50 mM. The gas products were then injected into a GC–MS (Perkin Elmer 680) equipped with a FID and a TCD. The mass fragments of ethylene were compared when ^{12}CO and ^{13}CO were used as reactants. The liquid products were analysed using ^{1}H NMR ('Electrochemical reduction product measurement').

The extent of ^{13}C labelling of each carbon was calculated by integrating the ^{13}C-induced split peaks. For example, in acetate, the peaks associated with the proton attached to the α carbon (the only NMR-visible proton) are the 1.8-ppm singlet corresponding to H-^{12}C and the 1.9- to 1.7-ppm doublet corresponding to H-^{13}C. The extent of ^{13}C labelling is obtained from:

$$\text{labelling extent}\,(\%) = \frac{\int I_{1.9\text{ppm}} + \int I_{1.7\text{ppm}}}{\int I_{1.9\text{ppm}} + \int I_{1.7\text{ppm}} + \int I_{1.8\text{ppm}}}$$

Data availability

All data are available from the authors on reasonable request. Source data are provided with this paper.

Acknowledgements

We acknowledge the support of this work by the Ontario Research Foundation—Research Excellence Program (number ORF-RE08-034, E.H.S.), the Natural Sciences and Engineering Research Council (NSERC) of Canada (number RGPIN-2017-06477, E.H.S.) and Suncor Canada. We acknowledge the support of the Government of Canada's New Frontiers in Research Fund (NFRF), CANSTOREnergy project, NFRFT-2022-00197. We thank R. Wolowiec, E. Palmiano and D. Kopilovic for their support in experimental set-up preparation. We thank W. Broomhead for his discussion on mechanistic pathways.

Author contributions

R.D. and E.S. designed the project under the supervision of E.H.S. R.D. and S.S. performed all the experiments. R.D. performed the isotope-labelling study and devised the mechanistic pathway. H.G.A. conducted the DFT study and wrote the relevant notes for that section. R.D. and S.S. wrote the first manuscript draft. R.D. and E.H.S. wrote

subsequent drafts of the manuscript. All authors contributed to discussion of the experimental results and manuscript preparation.

Competing interests

The authors declare no competing interests.

Additional information

Supplementary information The online version contains supplementary material available at https://doi.org/10.1038/s41557-025-01985-8.

Correspondence and requests for materials should be addressed to Edward H. Sargent.

Peer review information *Nature Chemistry* thanks Chen Peng and the other, anonymous, reviewer(s) for their contribution to the peer review of this work.